nature communications

Article

https://doi.org/10.1038/s41467-026-73604-0

Dual-domain metamaterials co-integrated with a compact ultrasonic transducer for highly directional audio generation

Received: 11 December 2025

Accepted: 15 May 2026

Published online: 22 May 2026

Check for updates

Woongji Kim [1,2,3,6], Beomseok Oh [1,6], Wonkyu Moon [1] & Junsuk Rho [1,3,4,5]

Directional audio systems, enabling personal sound sweet spots and spatially selective audio delivery, typically rely on parametric acoustic arrays that leverage nonlinear interactions of ultrasound beams to overcome the directivity constraint dictated by the wavenumber-aperture product. Such systems, known as parametric array loudspeakers (PALs), traditionally require phased arrays comprising tens to hundreds of ultrasonic emitters—posing persistent challenges for widespread adoption due to high cost, system complexity, and limited design flexibility. Here, we show an alternative form factor: a compact, single-body ultrasonic transducer integrated with dual-domain metamaterials, termed metamaterials-integrated parametric array loudspeakers (MiPALs). Unlike conventional PALs, the MiPAL utilizes a single piezoelectric driver co-integrated with dual-domain metamaterials—consisting of a co-designed acoustic metasurface and elastic meta-units—to yield a simple, cost-effective, and highly integrated architecture. To realize this, we exploit a unified design strategy that integrates theoretical modeling, metamaterial-transducer co-design, and comprehensive quantitative analyses of linear and nonlinear acoustic fields. Experiments demonstrate that the MiPAL generates ultra-broadband directional sound over four octaves, spanning from 500 Hz to 10 kHz. These findings underscore the potential of metamaterial-transducer co-integrated platforms for advanced audio systems, laying the foundation for immersive audio, spatial sound delivery, and extended reality.

Recent advancements in audio technologies have significantly enhanced spatial precision in sound reproduction[1,2], enabling immersive experiences such as personal surround audio, spatial sound zones (bright or/and dark)[3], and audio bubbles[4]. These capabilities are increasingly adopted across diverse platforms—including vehicle interiors, consumer electronics, and extended reality (XR) systems[5]. This growing demand for private and highly directional sound delivery has accelerated the need for compact sound sources capable of shaping and redirecting acoustic energy in space without affecting nearby listeners.

One promising approach to directional audio delivery is based on parametric arrays (PAs)[6–9], which leverage the nonlinear interaction of high-frequency ultrasonic beams in air to generate audible sound via difference-frequency wave (DFW) generation, also known as

[1]Department of Mechanical Engineering, Pohang University of Science and Technology (POSTECH), Pohang, Republic of Korea. [2]InnoCORE Research Center for Semiconductor Packaging Co-Physics Design Framework (SPACE-F), Ulsan National Institute of Science and Technology (UNIST), Ulsan, Republic of Korea. [3]POSCO-POSTECH-RIST Convergence Research Center for Flat Optics and Metaphotonics, Pohang, Republic of Korea. [4]Department of Chemical Engineering, Pohang University of Science and Technology (POSTECH), Pohang, Republic of Korea. [5]Department of Electrical Engineering, Pohang University of Science and Technology (POSTECH), Pohang, Republic of Korea. [6]These authors contributed equally: Woongji Kim, Beomseok Oh.
e-mail: wkmoon@postech.ac.kr; jsrho@postech.ac.kr

parametric down-conversion. This technique overcomes the fundamental directivity constraint imposed by the wavenumber-aperture product (ka)[10], which typically limits the applicability of conventional loudspeakers in compact directional audio systems. Unlike traditional devices that require physically large apertures to produce narrow beams at audible frequencies—due to the long wavelength of sound—parametric array loudspeakers (PALs) enable compact acoustic architectures capable of generating tightly confined audio beams (see Supplementary Note 1). These characteristics make PALs attractive for applications requiring spatially localized sound delivery, such as personal sound zones, and immersive audio in XR environments[2,5,11–14].

Despite the advantages of PALs, conventional implementations—commonly referred to as array-based PALs (APALs)[15–18]—face several inherent limitations. These include increased system complexity, stringent phase synchronization across multiple transducer elements, and high implementation costs, particularly when precise electrical amplitude and phase control are required to maintain beam quality[1]. In addition, APALs typically rely on off-the-shelf ultrasonic emitters such as Murata's MA40S4S[19], which operate typically at fixed center frequencies (e.g., 40 kHz). This reliance fundamentally limits design flexibility, as the transducer is conventionally treated as a given black-box source with predefined operating characteristics, rather than as a designable variable. Consequently, most prior studies have primarily focused on predicting nonlinear acoustic fields[3,16,18,20], while integrated design strategies—ranging from transducer architecture to nonlinear acoustic field generation—have remained largely underexplored. Recently, as an alternative to APALs, stepped-plate parametric array loudspeakers (SPPALs) have been proposed[21–24]. These systems employ a single piezoelectric transducer equipped with a flat plate modified by concentric annular steps, i.e., stepped-plate, enabling approximate phase compensation and emulating the coherent wavefront of an ideal rigid aperture source. While SPPALs have emerged as a compact PAL architecture, they also introduce additional challenges. The intricate step structures complicate transducer modeling and, when the step height becomes significant relative to the plate thickness, induce unwanted effects such as frequency shifts and undesired mode shapes[22]. These issues ultimately hinder the feasibility of systematic and predictable transducer designs. Furthermore, the inherent material damping often associated with integrated step structures—particularly those utilizing polymers—leads to significant efficiency degradation, representing a bottleneck for achieving sufficient sound volume (see Supplementary Note 16 for detailed discussion). Crucially, earlier SPPALs inevitably suffer from the compromise of their core functionality—directional sound reproduction—due to combination resonance (CR)[24]. This parasitic phenomenon, an inherent side effect of nonlinear intermodulation, generates nearly omnidirectional acoustic leakage that represents a primary drawback of existing single-body PAL architectures.

In this paper, we propose an alternative form factor for PALs—the metamaterials-integrated PAL (MiPAL)—which consists of a modular, single-body piezoelectric ultrasonic transducer co-integrated with dual-domain metamaterial architectures. Within this unified system, the acoustic metasurface serves as the primary functional layer; by leveraging subwavelength spatial resolution and high design flexibility, both considered well-known advantages of metamaterials[25–33], it effectively redirects the nondirectional ultrasound generated by the transducer's flexural vibration into a highly collimated and directional wavefront. As a result, directional audible sound is produced through DFW generation via nonlinear interactions of high-intensity ultrasonic waves. Simultaneously, the elastic meta-units act as a critical compensatory layer. By embedding deep-subwavelength locally resonant structures[34] onto the transducer's radiating plate, we effectively suppress the omnidirectional sound leakage associated with the CR mode that undermines the core functionality of the PAL by compromising its defining high directivity. To ensure the desired functionality and enable application-specific adaptability, we establish a unified design framework that facilitates the co-design of the transducer, acoustic metasurface, and elastic meta-units as an integrated device. This framework encompasses the comprehensive design of the MiPALs, integrating electromechanical transduction with dual-domain wave manipulation through theoretical investigation and rigorous full-field analyses of both linear and nonlinear behaviors in acoustic and elastic regimes. We fabricate a MiPAL prototype specifically designed for a representative target application scenario, and both experimentally and numerically validate its capability to generate highly directional audible sound across a broad frequency range of 500 Hz–10 kHz, covering over four octaves within the audible spectrum. Our approach effectively addresses the core limitations of existing approaches—including high system cost, structural complexity, and limited design flexibility—and establishes a clear pathway toward compact directional audio systems suitable for widespread deployment. Furthermore, by demonstrating deep sub-diffraction nonlinear wave manipulation[35] through device-level integration of metamaterials beyond conventional linear-wave-based approaches[36–38], this work highlights the potential of metamaterial–transducer co-integrated platforms, laying the groundwork for future applications in immersive audio, spatial sound delivery, and XR environments.

Results

Concept and overall principle of the MiPALs

Parametric acoustic arrays exploit the nonlinear properties of air to generate highly directional audible sound from high-intensity ultrasonic waves[6]. When a transducer emits two ultrasonic components at frequencies f_1 and f_2, their second-order nonlinear interaction in air forms a virtual end-fire line source at the difference frequency $|f_1 - f_2|$, producing a narrow audible beam that inherits the directivity of the ultrasonic primaries. Figure 1a schematically illustrates this principle, while Fig. 1b presents the corresponding frequency domain response, where two strong primary components give rise to a distinct difference-frequency peak as a result of air nonlinearity.

Conventional PALs are typically composed of multiple ultrasonic emitters, each with a fixed frequency response. Consequently, the source aperture is realized as a phased array with relatively large element spacing—often exceeding one wavelength[19]—which necessitates numerous emitters and results in increased system complexity and cost (see Supplementary Note 2 for details). In contrast, the proposed PAL architecture employs a single-body transducer integrated with metamaterial structures that provide modularity and design flexibility, enabling simplified configuration and customization. This modular approach facilitates straightforward assembly and disassembly while leveraging low-cost transducer elements and 3D-printable metamaterial components.

In the proposed system, a mechanical horn (see Fig. 1c) amplifies the vibrational displacement of a Langevin-type ultrasonic driver and excites the center of the wide-area radiating plate, inducing high-order flexural-mode vibration that generates an off-axis radiation pattern of ultrasonic fields (Fig. 1f, left). To convert this into a highly directional field, we integrate an acoustic metasurface (Fig. 1d) in front of the radiating plate, tailored to match the spatial characteristics of the flexural mode to make the coherent wavefront (Fig. 1f, right). This enables the desired high-ka collimated ultrasonic wave radiation, which undergoes a progressive nonlinear interaction in air to produce highly directional audio. However, during this process, unwanted parasitic vibrations can arise within the transducer structure. One such phenomenon, referred to as CR[39,40], occurs when intermodulation distortion components generated by multifrequency excitation drive the lower-order eigenmodes of the transducer in the audible range. The resulting parasitic radiation can reach sound pressure levels (SPLs)

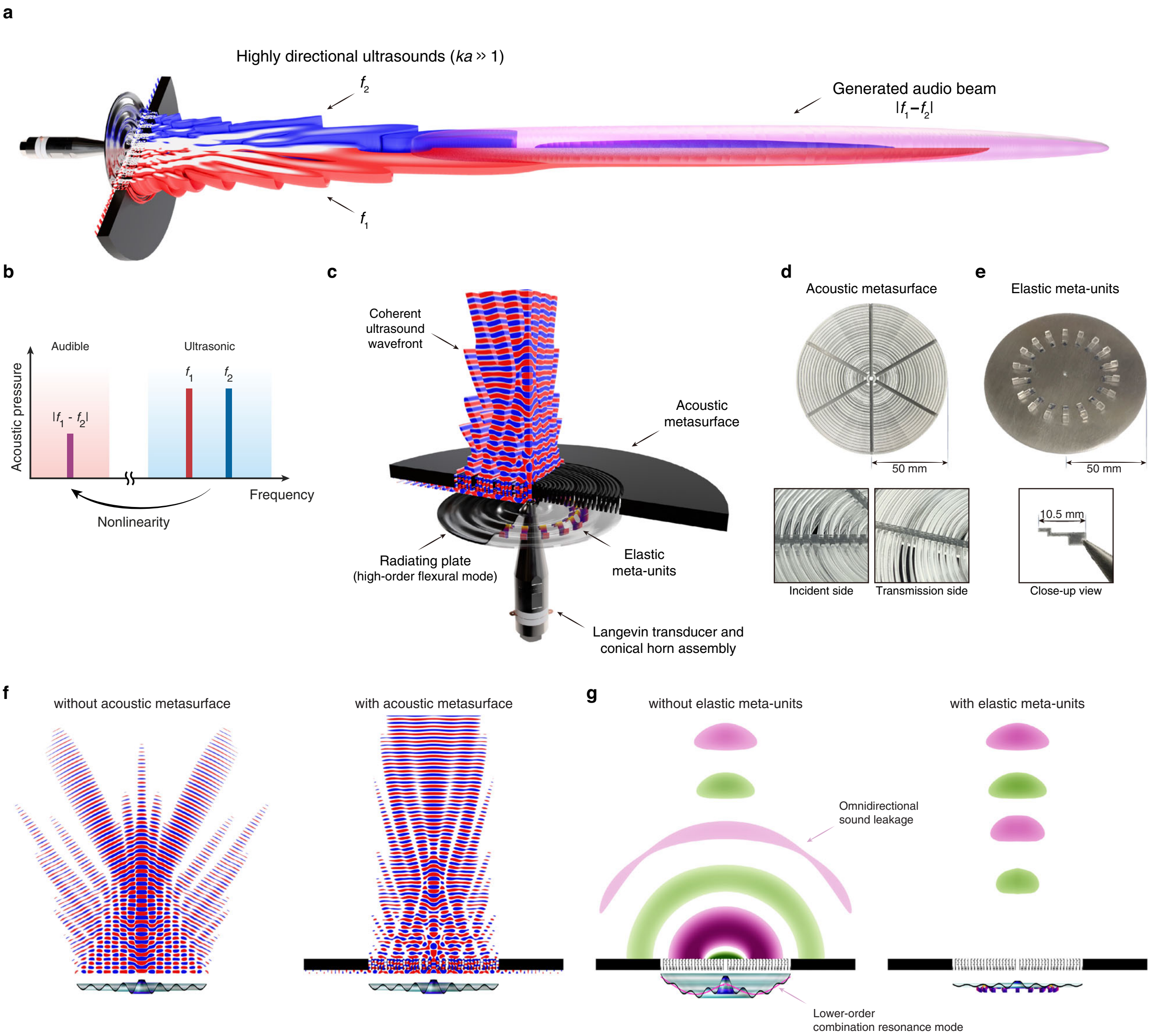

Fig. 1 | Overview of the metamaterials-integrated parametric array loudspeaker (MiPAL). a Schematic illustration of the MiPAL generating a directional ultrasonic field with high-*ka* (where *k* is the acoustic wavenumber and *a* the aperture radius) and a resulting secondary audible beam via nonlinear process. **b** Nonlinearity-enabled difference-frequency wave generation: two ultrasonic primary tones f_1 and f_2 interact in air to produce a demodulated audible component $|f_1 - f_2|$. **c** Schematic of the MiPAL architecture and coherent ultrasonic radiation mechanism. The device integrates a Langevin-type ultrasonic transducer, a conical mechanical horn, a large-area radiating plate, a metasurface for wavefront shaping, and elastic meta-units for undesired vibration suppression. **d** Photographs of the fabricated metasurface, illustrating (top) the 100 mm-diameter front view with axially symmetric phase-encoded layers supported by six radial ribs and (bottom) close-up views of the incidence and transmission sides that highlight the unit-cell design combining interconnected Helmholtz resonator arrays with a space-coiling channel. **e** Photographs of the radiating plate equipped with elastic meta-units, showing (top) the backside view with the meta-units attached to the plate and (bottom) a close-up view highlighting the local-resonance meta-unit geometry designed to form a bandgap that suppresses parasitic low-frequency omnidirectional radiation. **f** Visualized ultrasound fields without metasurface (left), showing incoherent radiation governed by the plate's flexural mode, and with metasurface (right), demonstrating collimated wavefront and high directivity. **g** Comparison of the secondary audio field influenced by structural vibration without elastic meta-units, parasitic combination resonance excites the plate's lower eigenmodes, producing omnidirectional leakage (left), and with elastic meta-units, these modes are effectively suppressed, resulting in a purely directional audio beam (right).

comparable to the intended on-axis output, producing a nearly omnidirectional acoustic leakage that masks the directional audible field and forms a virtual acoustic dome around the device (Fig. 1g, left). To suppress these parasitic phenomena, we attach deep-subwavelength elastic meta-units on the backside of the radiating plate (Fig. 1e), which are capable of effectively attenuating undesired structural vibrations by introducing a local-resonance bandgap near the lower-order mode frequency (Fig. 1g, right). Strategically designed to target the eigenfrequencies associated with CR, the elastic meta-units effectively mitigate the undesired dome effect, thereby preserving the directional audio output.

Design, characterization, and fabrication of the MiPALs

The design of the MiPALs revolves around integrating a monolithic ultrasonic transducer with acoustic and elastic meta-architectures to achieve the desired acoustic and mechanical responses for directional sound-beam generation. Each component is designed sequentially but becomes functionally co-integrated through structural integration within the overall device architecture. To assess the functionality and performance of the proposed form factor under realistic operating conditions, we develop a representative MiPAL configuration that reflects a typical use case in which the listener is positioned at a close distance (e.g., <1 m). Once the application-

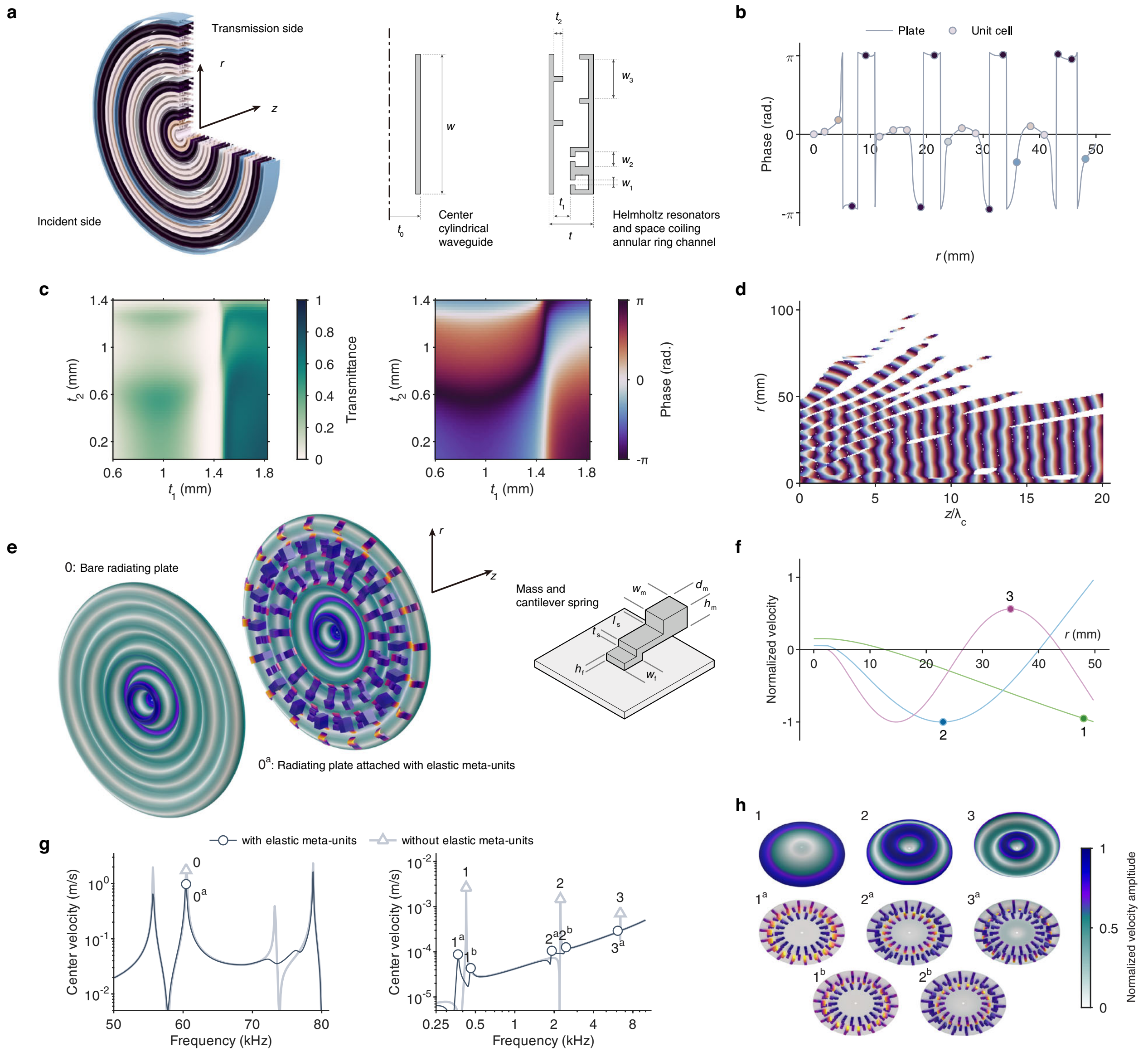

Fig. 2 | Design and characterization of the MiPAL. a Acoustic metasurface and its unit cells. Schematic of the metasurface colored according to the target phase distribution (left), consistent with **b** and **c**. Unit-cell configuration comprising a central waveguide and Helmholtz resonators connected through a space-coiling channel (right), where the geometric parameters (t = 2.43 mm, w = 8.58 mm, t_0 = 2.86 mm, w_1 = 0.3 mm, w_2 = 0.9 mm, t_1, t_2) define the acoustic response. **b** Radial phase profile for compensating incoherent high-order flexural-mode radiation from the plate. **c** Calculated transmittance (left) and phase (right) of the unit cell as functions of geometrical parameters. **d** Resulting coherent and directional ultrasonic wavefront in phase, where λ_c denotes the wavelength corresponding to the carrier frequency. **e** High-order flexural-mode plate and its elastic meta-units. Comparison of the radiating plate without and with attached elastic meta-units (left). Configuration of an elastic meta-unit (right), defined by the geometrical parameters (w_f = 3 mm, h_f = 1 mm, d_m = 3 mm, t_s, l_s, w_m). The foot and spring segments are integrated with a 1 mm longitudinal overlap. **f** Normalized mode shapes of the plate's low-order eigenmodes, indicating the target-attaching location of meta-units. **g** Frequency response of the transducer at the center of the plate with and without elastic meta-units in the ultrasonic range (left) and in the audible range (right). Superscripts a and b denote the lower- and higher-frequency split modes induced by the elastic meta-units. **h** Vibration-field distributions of the plate without and with elastic meta-units. Normalization is consistent within each modal family (e.g., 1, 1^a, 1^b) but not across different orders.

specific requirements—namely, aperture size and target hearing distance—are defined, the fundamental design parameters—such as radiator thickness and ultrasonic carrier frequency—can be determined based on nonlinear acoustic analysis (see Supplementary Note 3 for details). These parameters serve as the foundation for the subsequent design of the Langevin transducer, mechanical horn, and radiating plate, ensuring the desired acoustic output and beam characteristics (see Supplementary Note 4 for detailed transducer design).

Based on the preliminary-established design process (Supplementary Notes 3 and 4), we proceed to design the acoustic metasurface with a 60 kHz carrier frequency, a 100 mm aperture diameter, and a 0.5 m target hearing distance. The radiating plate of the transducer is identical in size, with a diameter of 100 mm, aligning with the metasurface aperture. For its implementation, we adopt and tailor a hybrid unit-cell geometry[41,42] comprising radially arranged Helmholtz resonators (HRs) interconnected by a space-coiling (SC) channel (Fig. 2a). The design parameters t_1 and t_2 are adjusted to control the cavity volumes of HRs and the length and volume of the SC channel, respectively, achieving the desired transmittance and phase. It is noteworthy that the central (innermost) unit cell employs a pure waveguide channel to overcome poor impedance match arising from its inherently limited acoustic volume (see "Methods" for details on the unit-cell design).

To achieve desired wavefront shaping, each unit cell is individually encoded to compensate for the incoherent radiation modes produced by the radiating plate (Fig. 2b), ensuring accurate phase modulation and high transmission at the center frequency (see Supplementary Note 5 for details). Figure 2c presents the calculated transmittance and phase of the unit cells as functions of the design parameters. By mapping the required phase profile, the metasurface enables coherent and collimated beam formation. The designed metasurface was subsequently fabricated using high-resolution stereolithography (SLA) 3D printing (Fig. 1d; fabrication details provided in "Methods"). The efficacy of the metasurface-enabled wavefront shaping is further verified by analyzing the spatial phase profiles along the propagation axis (Fig. 2d). Immediately after transmission through the metasurface, the wavefront exhibits transient oscillatory phase variations due to near-field nonlocal coupling effects. However, after propagating over several wavelengths, it clearly forms a planar wavefront, confirming directional beam generation in the high-*ka* regime.

In parallel, to mitigate unintended excitation of the plate's lower-order flexural modes—which otherwise deteriorate directivity—we attach elastic meta-units at strategically chosen sites on the radiating plate (Fig. 2e). Each meta-unit consists of a cantilever spring connected to a concentrated inertial mass, parameterized by (w_f, h_f, t_s, l_s, w_m, d_m, h_m). This architecture functions as a locally resonant metamaterial that is weakly coupled to the host plate, thereby providing mode-selective loss. When the local resonance of a meta-unit is tuned near a targeted plate mode, the effective dynamic properties experienced by that mode are altered and additional dissipation is introduced, reducing its amplitude while minimally penalizing the high-order operating mode used for ultrasonic radiation (see Supplementary Note 7 for details on design and characterization of elastic meta-units).

We calculate the plate's dominant lower-order eigenmodes and select attachment locations to coincide with the antinodal lobes where strain energy concentrates (Fig. 2f). The efficacy of this strategy is evidenced by the frequency response measured at the plate center using a laser Doppler vibrometer (LDV), with and without the elastic meta-units, under transducer drive (Fig. 2g). In the ultrasonic band (left panel), the intended resonance and radiation efficiency are nearly preserved—a consequence of the weak coupling between the meta-units and the high-order mode used for beamforming with the acoustic metasurface. In the audible band (right panel), the lower-order resonances exhibit pronounced peak reduction and broader bandwidth ($1 \rightarrow 1^a, 1^b$; $2 \rightarrow 2^a, 2^b$; $3 \rightarrow 3^a$), indicating mode splitting and increased damping, where the superscripts a and b denote the lower- and higher-frequency split modes, respectively. The plate's vibration-field maps (Fig. 2h) further visualize the effect of the elastic meta-units, with an enlarged and more detailed representation provided in Supplementary Fig. 17. Without meta-units, the field contains noticeable lower-order mode patterns; after attachment, these patterns are strongly attenuated. Together with Fig. 2g, these observations confirm that the elastic meta-units selectively suppress detrimental modes while maintaining the coherent ultrasonic output necessary for directional audio.

Experimental characterization of the MiPAL

To evaluate the acoustic performance of the fabricated MiPAL, acoustic field measurements were conducted in a semi-anechoic chamber using the experimental setup shown in Fig. 3a. The metasurface was mounted at a distance of $\lambda_c/2$ from the radiating plate, where λ_c denotes the wavelength corresponding to the carrier frequency. During all measurements, the transducer was driven at an input voltage of 50 V. A 1/8″ microphone was employed for ultrasonic measurements. All measurements were systematically performed by scanning the microphone mounted on an automated linear stage, while simultaneously rotating the transducer with an automated rotational stage (see "Methods" and Supplementary Note 9 for details).

For the ultrasonic field, we first present the spatial propagation curves corresponding to the 60 kHz carrier and five upper-sideband tones offset by 0.5, 1, 2, 4, and 8 kHz that produce the corresponding audio frequencies (see Fig. 3b and Supplementary Fig. 20 for detailed spectra). Both experimental and numerical results confirm that the ultrasound SPL peaks at approximately 0.45 m, slightly upstream of the 0.5 m target hearing distance at which the demodulated secondary audio field is concentrated through cumulative nonlinear effects[19] (see "Methods" and Supplementary Notes 3 and 8 for simulation details). The broadband performance of the MiPAL is further demonstrated through frequency response analysis and beam patterns (Fig. 3c, e). The MiPAL maintains high SPL across 10 kHz ultrasonic frequency span, ensuring reliable acoustic performance for the audible range. This capability arises from the acoustic responses of the constituent meta-atoms, which exhibit reasonable transmittance over the operating frequency range (see Supplementary Note 6 for details).

The directional characteristics of the ultrasonic field were examined by comparing the beam patterns obtained without and with the acoustic metasurface (Fig. 3d, e). The beam patterns were measured in a radial manner at a distance of 0.45 m from the MiPAL using a rotational stage. Without the metasurface, the radiating plate exhibits an off-axis radiation pattern, indicating poor collimation. In contrast, the introduction of the metasurface substantially enhances beam directivity, producing a sharply confined main lobe along the propagation axis (additional beam patterns at representative frequencies are provided in Supplementary Figs. 8 and 22). This improvement arises from the frequency-dependent phase gradients imparted by the metasurface, which closely follow the dispersion characteristics of the flexural plate, thereby enabling broadband phase modulation without introducing significant wavefront distortion (Supplementary Note 6). As a result, the MiPAL exhibits pronounced directional characteristics, with sharp directivity observed in the upper ultrasonic frequency range (60–70 kHz), whereas the lower band (50–60 kHz) shows comparatively weaker directivity. We note that this structural-phase compatibility between the metasurface and the radiating plate facilitates broadband directional beam formation. Importantly, this bandwidth further extends into the audio frequency range, enabling directional sound beam formation across more than four octaves—from 500 Hz to 10 kHz. Whereas conventional acoustic metasurfaces are often narrowband because their dispersion control relies on the resonance-based sound-speed modulation, our approach sidesteps this limitation: the metasurface and the transducer are engineered to generate the directional ultrasound carriers, and nonlinear interaction-enabled difference-frequency generation maintains the high-*ka* directivity into the audio band. In effect, the interplay between the collimated ultrasounds and nonlinear interaction produces a deep sub-diffractive sound manipulation with expanded bandwidth, overcoming the limitations of conventional metasurfaces in the linear regime[43–46]. Nevertheless, we also note that owing to the inherent dispersive nature of both the acoustic metasurface and the transducer, chromatic (frequency-dependent) aberrations may arise, potentially distorting the wavefront across the operational bandwidth. These effects are discussed in detail in Supplementary Note 6, and can be mitigated using advanced dispersion-engineering techniques[47–49]. However, we emphasize that in integrated systems such as the MiPAL, it is essential to simultaneously account for not only the metasurface's intrinsic dispersion but also the transducer's structural dispersion—a complex interplay that represents a significant leap from conventional metasurface design and will be a key subject of our future study.

To further characterize the audible field generated through nonlinear acoustic interaction, we measured the demodulated audio signals using a 1/2" microphone equipped with a spurious-sound filter that suppresses intermodulation distortion within the microphone itself, thereby ensuring that only the true difference-frequency

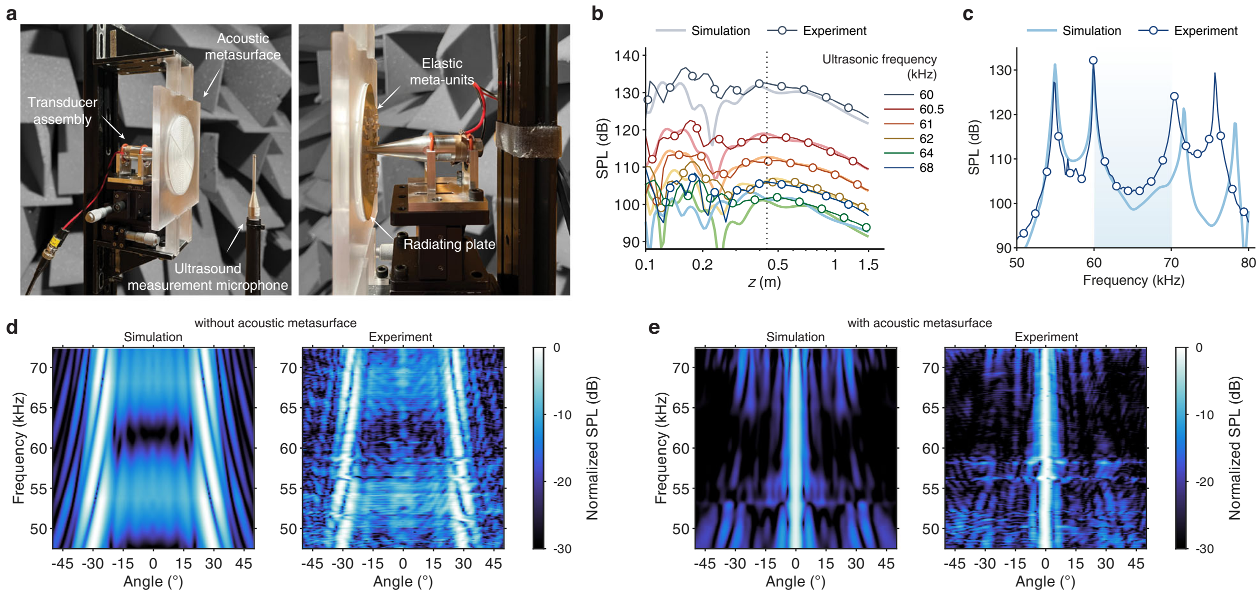

Fig. 3 | Evaluation of the ultrasound characteristics. a Experimental setup for measuring ultrasonic fields in a semi-anechoic chamber, showing the transducer prototype with the acoustic metasurface (left) and the elastic meta-units attached to the radiating plate (right). **b** Simulated and measured propagation curves at six primary ultrasonic frequencies (60, 60.5, 61, 62, 64, and 68 kHz). The ultrasound SPL peaks near 0.45 m (dotted vertical line); cumulative nonlinear interaction then yields the demodulated audio peak at the 0.5 m target hearing distance (see Fig. 4b). **c** Simulated and measured SPL as a function of frequency. Blue shaded region indicates operating frequency range. **d, e** Directivity patterns (simulation and experiment) at 0.45 m comparing configurations without and with the acoustic metasurface. **d** Without the metasurface, the ultrasonic field exhibits off-axis radiating patterns governed by flexural-mode radiation of the plate. **e** In contrast, the metasurface-integrated configuration produces a highly collimated beam across the 60–70 kHz range, confirming the effectiveness of metasurface-enabled wavefront shaping and broadband directivity.

components are captured (Fig. 4a and see Supplementary Note 10 for details). To realize highly directional difference-frequency audio signals with suppressed side lobes, an upper-sideband amplitude modulation scheme is adopted (see Supplementary Note 6 for details). Figure 4b presents the propagation curves of representative audio frequencies (0.5, 1, 2, 4, and 8 kHz). The acoustic pressure peaks at a critical distance of approximately 0.5 m, defined as the hearing distance, where the secondary audio field attains its maximum intensity (see Supplementary Note 3). The numerical simulations for the nonlinear acoustic field follow the quasi-linear approximation to the Westervelt equation (see "Methods" and Supplementary Note 8 for details). At this hearing distance, the measured and simulated SPLs as a function of audio frequency (Fig. 4c) confirm broadband audio generation extending from 0.5 to 10 kHz. The corresponding beam patterns (Fig. 4d) compare the combination-resonance-free simulation with measurements obtained with and without elastic meta-units. The results demonstrate that the embedded meta-units effectively suppress CR within the audible range, thereby preserving the high directivity of the audio field. The quantified discrepancy in Supplementary Fig. 21 further demonstrates that the meta-units effectively align experimental performance with theoretical predictions by suppressing parasitic CR modes. The frequency-dependent half-power beamwidth (HPBW) shown in Fig. 4e further confirms the broadband nature of the directional beam across the 0.5–10 kHz range. Representative beam patterns at selected frequencies illustrate excellent agreement between simulation and experiment (Fig. 4f). Notably, at 2 kHz—where CR tends to induce omnidirectional sound leakage by the bare radiating plate—the elastic meta-units effectively suppress this parasitic radiation, maintaining the collimated beam structure. These results collectively confirm that the nonlinear acoustic field of the designed MiPAL can be accurately predicted, enabling optimization for specific application requirements. Furthermore, the acoustic metasurface serves to convert the high-order flexural-vibration-induced incoherent wavefront into a collimated wavefront, while the elastic meta-units effectively suppress the parasitic excitation of lower-order modes.

Potential applications of the MiPALs

Due to its compact form factor and scalability, the MiPAL architecture can be well suited for deployment in confined environments such as aircraft cabins (Fig. 5a). Unlike traditional APALs, its space-efficient design allows for seamless integration into seating areas where per-unit cost and mounting volume are critical constraints. In such settings, MiPALs can facilitate personal sound delivery with minimal crosstalk between nearby listeners. To demonstrate this capability, we performed a speech-based experiment in a controlled anechoic environment—consistent with the measurement setup in Fig. 4a—for a rigorous characterization of the intrinsic properties of the MiPAL, free from any external environmental factors. Recording was conducted at a distance of 0.5 m and at the angles (0°, 15°, 30°, 45°) defined in Fig. 5b. The audio source is a readily accessible subway announcement and its spectrogram is shown in Fig. 5c. Figure 5d presents the spectrograms of the demodulated audio recorded at the angles in Fig. 5b. As expected from directional patterns, off-axis levels decrease with increasing angle. A high-intensity horizontal band appears in the spectrogram near 2 kHz when elastic meta-units are absent (right column), indicating omnidirectional sound leakage due to the CR; with elastic meta-units (left column), this component is strongly suppressed—consistent with the swept-frequency response analysis in Fig. 5e.

Figure 5f summarizes level metrics: (top) time-weighted SPL (A-weighted); (bottom) off-axis levels normalized by the on-axis (0°) signal at the tested angles. With elastic meta-units, parasitic effects are effectively suppressed, allowing the beam directivity to be preserved. We further evaluated MiPAL performance with diverse speech and music program materials (see Supplementary Note 12 for details). Figure 5e shows the (log-chirp) swept-frequency responses at the tested angles, each normalized to the on-axis response. Near the

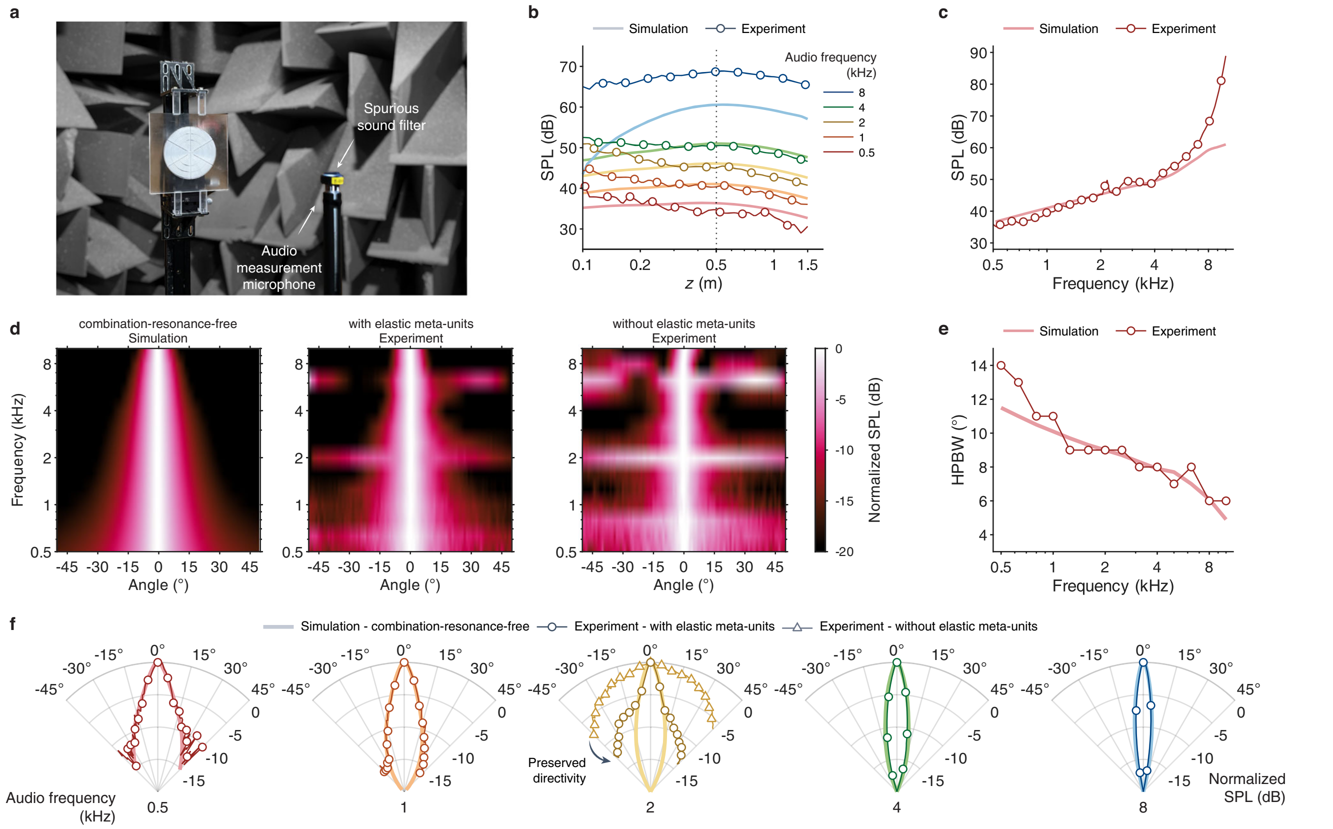

Fig. 4 | Audio characteristics arising from nonlinear acoustic interaction. **a** Experimental setup for measuring the audible field in a semi-anechoic chamber. The MiPAL was driven by two ultrasonic primary tones, while an audio microphone equipped with a spurious-sound filter was used to capture only demodulated audio signals. **b** Propagation curves at representative audio frequencies (0.5, 1, 2, 4, and 8 kHz). The SPL peaks near 0.5 m correspond to the designated target hearing distance (dotted line). **c** Comparison of simulated and measured SPL as a function of audio frequency, showing broadband audio generation over 0.5–10 kHz. **d** Audio directivity at the target hearing distance (0.5 m): combination-resonance-free simulation (left), and measured directivity with (middle) and without (right) elastic meta-units. **e** Calculated and measured frequency response of half-power beam-width (HPBW), confirming the high directivity. **f** Beam patterns at the target hearing distance (0.5 m) for selected audio frequencies (0.5, 1, 2, 4, and 8 kHz), illustrating highly directional beams over four octaves of operation.

second-order CR band at approximately 2 kHz, the case with elastic meta-units stays below 0 dB and decreases further as the angle increases. By contrast, the case without elastic meta-units remains above 0 dB and shows negligible angular variation across the off-axis responses. The first- and third-order CRs (around 400 Hz and 6 kHz; see the right panel of Fig. 2g) fall outside the targeted suppression band in this implementation, which was tuned to the second-order CR (near 2 kHz); consequently, little or no attenuation is observed in those ranges. Additional experiments and analyses detailed in Supplementary Notes 12 and 13, and Supplementary Movies 1–5 demonstrate the generality of performance essential for a practical personal audio device, specifically highlighting the improved clarity achieved through the effective suppression of ringing by the elastic meta-units.

Altogether, the proposed MiPAL architecture enables cost-effective, broadband personal sound delivery and offers the scalability required for large-scale in-cabin deployment. Beyond stationary uses, we envision high potential for its adoption in various portable and compact audio applications.

Discussion

In this work, we introduce the MiPAL, which fundamentally redefines the architecture for advanced personal audio systems through the dual-domain integration of metamaterials. By synergistically combining an acoustic metasurface and elastic meta-units with a compact single-body ultrasonic transducer, the MiPAL achieves broadband directional sound generation without relying on costly multi-emitter arrays or the complex phase-control electronics typically required in conventional systems[1,19]. The metasurface redirects the incoherent flexural-mode radiation into collimated wavefronts, while embedded elastic meta-units effectively suppress parasitic vibration modes that otherwise cause undesired omnidirectional leakage. As a result, the MiPAL demonstrates directional audio performance across an ultra-broad frequency range from 500 Hz to 10 kHz—covering over four octaves within a physically compact platform. Our approach overcomes the cost, complexity, and scalability limitations of conventional PALs, paving the way for widespread adoption in diverse applications.

Despite these promising advances, several challenges remain. The current prototype still produces a relatively limited SPL compared to conventional loudspeakers, primarily constrained by the inherently low nonlinear conversion efficiency of parametric arrays; a quantitative power-flow analysis is provided in Supplementary Note 15. Further optimization is therefore required to achieve sufficient SPL for personal listening applications, where preferred levels typically reach approximately 70 dBA[50]. Beyond SPL enhancement, the modular design strategy offers opportunities for application-specific customization, enabling tailored solutions for diverse acoustic environments. Future studies exploring the metamaterial–transducer co-integrated configurations will be essential to improve versatility across different application environments.

Looking ahead, such physically compact, portable, and readily customizable platforms could enable spatial sound delivery in next-generation immersive audio and XR applications. Furthermore, we foresee that the interweaving of architected metamaterials with real-world functional platforms will drive transformative advances across

 https://doi.org/10.1038/s41467-026-73604-0

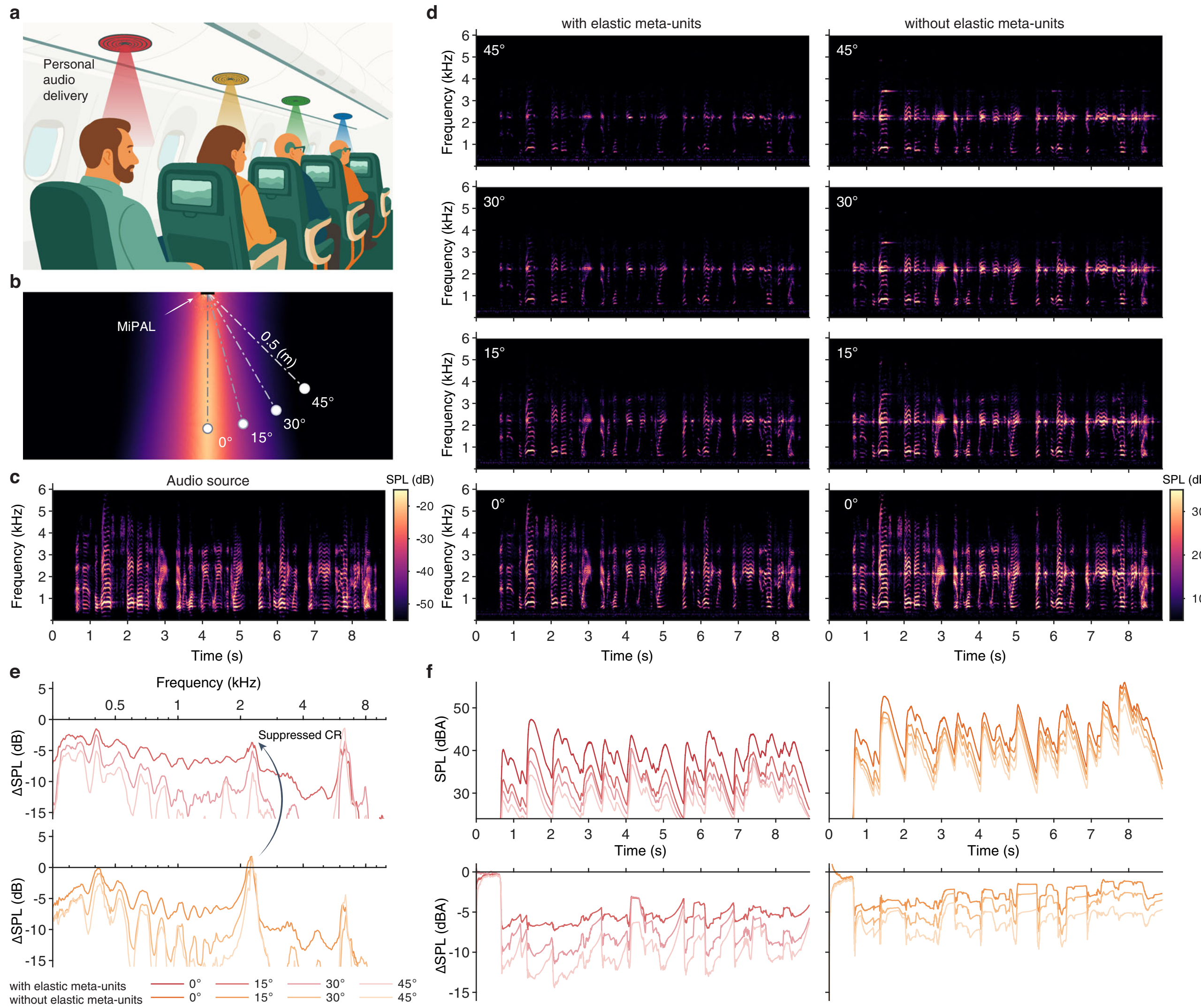

Fig. 5 | Potential applications of the MiPALs. a Conceptual illustration of in-cabin (e.g., aircraft or train cabin) personal sound delivery, enabling independent media streams with minimal crosstalk. **b** Geometry for the speech demonstration at 0.5 m conducted in an anechoic chamber: microphones at 0°, 15°, 30°, 45°. **c** Spectrogram of the original speech source. **d** Spectrograms of recorded audio at the angles in (**b**), with elastic meta-units (left), without (right); a common color scale (single colorbar) is used across panels. In the case without elastic meta-units, omnidirectional sound leakage near 2 kHz due to combination resonance (CR) is observed, consistent with (**e**). **e** Swept-frequency (log-chirp) responses at the angles in (**b**), each normalized to the on-axis response. **f** Time-weighted SPLs (top); off-axis levels (bottom) normalized by the on-axis signal, with elastic meta-units (left), without (right). Panels (**e**) and (**f**) share the same color legend for the measurement angles.

diverse fields, including biomedicine, nondestructive testing, and energy harvesting, by enabling unprecedented control over wave–matter interactions.

Methods

Fabrication of transducer, acoustic metasurface, and elastic meta-units

The architecture of the Langevin-type piezoelectric wide-area plate transducer is illustrated in Supplementary Fig. 5. The transducer consists of a backing tail (stainless steel), piezoelectric rings (PZT-82; Sino Sonics), a matching head (aluminum), a conical-shaped mechanical horn (aluminum), and a radiating plate (aluminum). Except for the piezoelectric rings, all components were fabricated via precision computer numerical control (CNC) lathe. For assembly, the backing tail, piezoelectric rings, and matching head were first assembled to form the Langevin-type configuration. The mechanical horn (conical section) was then coupled to the Langevin transducer. During this process, a custom-designed clamping jig was employed to securely hold the transducer under mechanical bias, while a dedicated alignment tool was used to ensure coaxial alignment between the piezoelectric rings and the transducer body. To achieve consistent mechanical preloading, a torque wrench (CL15NX8D; Tohnichi) was used to apply a controlled torque to the central bolt. Finally, the radiating plate—with elastic meta-units pre-embedded—was attached to the horn using a bolt. Further details about the transducer assembly are provided in Supplementary Note 14.

The acoustic metasurface and elastic meta-units were fabricated using an SLA 3D printing method with a resolution of 0.05 mm. The material used was a photo-polymer UV resin (Accura ClearVue; 3D Systems). The metasurface consists of 21 layers of unit cells, with the minimum wall thickness fixed at 0.3 mm. To ensure structural stability of the axially symmetric unit-cell layers, six radial ribs—each with a thickness of 1.5 mm—were added to reinforce the structure. Additionally, a 150 × 150 mm rectangular structure (baffle) was included around the circular metasurface to improve mounting stability. For the elastic meta-units, a total of 18 units were attached on the plate.

Numerical simulations

The full-wave simulations were conducted using a finite element method (FEM) based on the commercial software, COMSOL Multiphysics 6.2. The mass density and sound speed of the background medium (air) are 1.21 kg m^{-3} and 343 m s^{-1}, respectively. To design the meta-atoms considering narrow-channel loss effects, the viscous-thermal boundary layer effect was incorporated. For the thermoviscous acoustic modeling, we used typical parameters of air, including a specific heat ratio of 1.4, thermal conductivity of 0.0263 W m^{-1} K^{-1}, heat capacity at constant pressure of 1.005 kJ kg^{-1} K^{-1}, and dynamic viscosity of 1.81×10^{-5} Pa s. The acoustic metasurface was designed to have an axisymmetric geometry and was modeled in cylindrical coordinates. To design the meta-atom, we calculated transmission and phase characteristics based on the parameter retrieval method[51] using the scattering matrix. The simulations were conducted on a supercell[52] composed of 20 identical geometries radially distributed along an axisymmetric configuration. The unit-cell geometries were selected to span the required phase-shift range while maintaining a phase-deviation tolerance below 0.01 rad (see Supplementary Note 5 for details). As discussed, the central unit cell consists of a simple waveguide structure, and all remaining meta-atoms were designed to satisfy the required relative phase shifts with respect to the center unit cell.

The methods for calculation of nonlinear acoustic fields employed in this study are based on the successive approximation of the Westervelt equation. The theoretical foundations are detailed in Refs. 53–55. In particular, the quasi-linear approximation ($\varphi(r, t) = \varphi_1(r, t) + \varphi_2(r, t)$, where φ indicates the acoustic variable, φ_1 represents the primary ultrasonic, and φ_2 represents the secondary audio field) to the Westervelt equation is adopted, which enables tractable yet reasonably accurate computation of the difference-frequency field[54,55]. The governing model equation is as follows:

$$\nabla^2 p - \frac{1}{c_0^2}\frac{\partial^2 p}{\partial t^2} + \frac{\delta}{c_0^4}\frac{\partial^3 p}{\partial t^3} = -\frac{\beta}{\rho_0 c_0^4}\frac{\partial^2 p^2}{\partial t^2}, \tag{1}$$

where p is the acoustic pressure, c_0 is the small-signal sound speed, ρ_0 is the mass density, δ is the sound diffusivity, and β is the nonlinear coefficient.

Under the quasi-linear approximation in the frequency domain, Eq. 1 reduces to a coupled set of homogeneous and inhomogeneous Helmholtz equations:

$$\nabla^2 p_i + k_i^2 p_i = 0, \tag{2}$$

$$\nabla^2 p_\mathrm{a} + k_\mathrm{a}^2 p_\mathrm{a} = \frac{4\pi^2 \beta f_\mathrm{a}^2}{\rho_0 c_0^4} p_1^* p_2, \tag{3}$$

where $i = 1, 2$ denote the primary ultrasonic frequencies ($f_2 > f_1$), the difference (audio) frequency is $f_\mathrm{a} = f_2 - f_1$, and the asterisk represents the complex conjugate. We solved these equations using two numerical frameworks: the full FEM approach and the hybrid FEM-SWE approach, with detailed methodologies for the nonlinear field analysis described in Supplementary Note 8. For the background medium, atmospheric attenuation was incorporated in the FEM model following ISO 9613-1[56] under a relative humidity of 70% and a temperature of 20°C.

Acoustic field measurements

All acoustic measurements were conducted in a semi-anechoic chamber with a free-field effective volume of 3 m × 3 m × 2 m. The chamber had an average absorption coefficient of 0.99, a low-frequency cutoff of 150 Hz, and a background noise level of approximately 30 dB SPL. Temperature and relative humidity were maintained at 20°C and 70%, respectively.

The MiPAL was mounted on a motorized rotational stage using a custom-designed jig and positioned 1.4 m above the chamber floor. The transducer was driven by a dynamic signal analyzer (SR785; Stanford Research Systems) through a power amplifier (HSA4052; NF Corporation). A 1/8″ microphone (Type 4138; Brüel & Kjær) and a 1/2" microphone (Type 4192; Brüel & Kjær) were used for ultrasound and audio sound measurements, respectively. Each microphone was mounted on a single-axis motorized linear translation stage via a custom-built interchangeable holder to enable high-precision spatial scanning. The measured acoustic signals were amplified using a conditioning amplifier (Nexus 2690; Brüel & Kjær) and subsequently recorded using a dynamic signal analyzer (SR785; Stanford Research Systems). MATLAB 2024b was employed for data acquisition and synchronization and control of all instruments. Further details on experimental setup are provided in Supplementary Note 9. For audio-performance experiments (Supplementary Notes 12 and 13), the upper-sideband amplitude-modulation signals were numerically generated in MATLAB 2024b and converted to analog drive signals and synchronously acquired using a data acquisition device (USB-6361; National Instruments).

For ultrasound measurements, the microphone was positioned at a 90° angle of incidence to the propagating direction to facilitate free-field correction. For audible sound measurements, a hybrid configuration was employed: the microphone was positioned at 90° and coupled with an acoustic filter assembly, following the approach proposed in our previous work[57]. This method effectively mitigates undesired spurious sound in complex near-field environments, thereby ensuring accurate acquisition of the audio pressure field (see Supplementary Note 10 for details).

Vibration characteristics measurements

To evaluate the vibrational characteristics of the transducer and elastic meta-units, the device was affixed to a custom-built mounting jig. The surface velocity of the plate was measured using a laser Doppler vibrometer (LDV; OFV-505 sensor head, OFV-5000 controller, VD-09 decoder; Polytec). For spatially resolved measurements (flexural mode shapes), the LDV sensor head was automatically scanned along the radial axis of the plate using two motorized linear translation stages arranged in series (LTA-HS; Newport). The motion of the stages was precisely controlled by a dedicated motion controller (ESP301; Newport), enabling precise scanning. The transducer was electrically excited using a signal analyzer (SR785; Stanford Research Systems) connected through a power amplifier (HSA4052; NF Corporation), the corresponding vibrometer output was concurrently acquired. All equipment, including motion control, signal generation, and data acquisition, was synchronized and automated using custom MATLAB 2024b scripts. Further details regarding the vibration measurement setup are provided in Supplementary Note 11.

To characterize the elastic meta-units (see Supplementary Note 7 for details), each unit was mounted on a custom jig and excited using a vibration exciter (Type 4810; Brüel & Kjær), while the velocity of the mass element was measured with a single-point LDV (OFV-511, OFV-3000; Polytec) to identify its local-resonance frequency. The mechanical impedance of the radiating plate, in both the bare and meta-unit-integrated configurations, was measured using an impedance head (288D01; PCB Piezotronics) mounted at the center.

Data availability

All technical details for reproducing the figures are provided in the manuscript and the Supplementary Information. The underlying measurement data are available from the corresponding authors on request.

Code availability

All technical details for implementing the simulations and analyses are provided in the manuscript and the Supplementary Information. The custom scripts for measurement automation and analysis are available from the corresponding authors on request.

References

1. Melde, K., Mark, A. G., Qiu, T. & Fischer, P. Holograms for acoustics. *Nature* **537**, 518–522 (2016).
2. Zhang, H., Wang, Q., Fink, M. & Ma, G. Optimizing multi-user indoor sound communications with acoustic reconfigurable metasurfaces. *Nat. Commun.* **15**, 1270 (2024).
3. Zhong, J.-X., Ji, J., Xia, X., Heo, H. & Jing, Y. Audible enclaves crafted by nonlinear self-bending ultrasonic beams. *Proc. Natl. Acad. Sci. U.S.A.* **122**, e2408975122 (2025).
4. Chen, T., Itani, M., Eskimez, S. E., Yoshioka, T. & Gollakota, S. Hearable devices with sound bubbles. *Nat. Electron.* **7**, 1047–1058 (2024).
5. Betlehem, T., Zhang, W., Poletti, M. A. & Abhayapala, T. D. Personal sound zones: delivering interface-free audio to multiple listeners. *IEEE Signal Process. Mag.* **32**, 81–91 (2015).
6. Westervelt, P. J. Parametric acoustic array. *J. Acoust. Soc. Am.* **35**, 535–537 (1963).
7. Bennett, M. B. & Blackstock, D. T. Parametric array in air. *J. Acoust. Soc. Am.* **57**, 562–568 (1975).
8. Gan, W.-S., Yang, J. & Kamakura, T. A review of parametric acoustic array in air. *Appl. Acoust.* **73**, 1211–1219 (2012).
9. Guo, Y. Directional sound propagation in acoustic artificial structures. *npj Acoust.* **1**, 8 (2025).
10. Blackstock, D. T. *Fundamentals of Physical Acoustics* (John Wiley & Sons, 2000).
11. Hamilton, M. F. in *Nonlinear Acoustics* (eds Hamilton, M. F. & Blackstock, D. T.) Ch. 8 (Springer Nature, 2024).
12. Hu, B. et al. Non-Hermitian topological whispering gallery. *Nature* **597**, 655–659 (2021).
13. Wen, X., Cho, C., Zhu, X., Park, N. & Li, J. Nonreciprocal field transformation with active acoustic metasurfaces. *Sci. Adv.* **10**, eadm9673 (2024).
14. Shi, C. & Gan, W.-S. Development of parametric loudspeaker. *IEEE Potentials* **29**, 20–24 (2010).
15. Yoneyama, M., Fujimoto, J.-I., Kawamo, Y. & Sasabe, S. The audio spotlight: an application of nonlinear interaction of sound waves to a new type of loudspeaker design. *J. Acoust. Soc. Am.* **73**, 1532–1536 (1983).
16. Zhong, J. et al. Low frequency audio sound field generated by a focusing parametric array loudspeaker. *IEEE-ACM Trans. Audio Speech Lang. Process.* **30**, 3098–3109 (2022).
17. Yang, J. & Ji, P. *Parametric Array Loudspeakers: From Theory to Application* (Springer, 2025).
18. Zhuang, T., Li, M., Li, S., Zhong, J.-X. & Lu, J. Wideband sound reproduction using a massive multi-channel focusing parametric array loudspeaker system. *J. Acoust. Soc. Am.* **158**, 3339–3347 (2025).
19. Zhong, J. & Qiu, X. *Acoustic Waves Generated by Parametric Array Loudspeakers* 1st edn (CRC Press, 2024).
20. Li, S.-Z., Zhuang, T., Zhong, J.-X. & Lu, J. Extended King integral for modeling of parametric array loudspeakers with axisymmetric profiles. *J. Acoust. Soc. Am.* **156**, 2189–2199 (2024).
21. Hwang, Y. & Moon, W. A wide-band in-air parametric array source composed of a circular plate with steps and a Langevin transducer with a horn. *Appl. Acoust.* **141**, 223–233 (2018).
22. Kim, C., Hwang, Y., Shin, K. & Moon, W. A parametric array loudspeaker featuring a Langevin transducer, a circular aluminum plate, and composite polymer steps. *Sens. Actuators A-Phys.* **338**, 113466 (2022).
23. Oh, B., Kim, C., Lee, D., Rho, J. & Moon, W. An improved analytic model for designing the polymer-composite stepped-plate transducer using the modified Mindlin plate theory. *Ultrasonics* **131**, 106933 (2023).
24. Kim, W., Oh, B., Kim, C. & Moon, W. Design, analysis, and experimental validation of a stepped plate parametric array loudspeaker. *J. Acoust. Soc. Am.* **158**, 2561–2576 (2025).
25. Cummer, S. A., Christensen, J. & Alù, A. Controlling sound with acoustic metamaterials. *Nat. Rev. Mater.* **1**, 16001 (2016).
26. Ma, G. & Sheng, P. Acoustic metamaterials: from local resonances to broad horizons. *Sci. Adv.* **2**, e1501595 (2016).
27. Assouar, B. et al. Acoustic metasurfaces. *Nat. Rev. Mater.* **3**, 460–472 (2018).
28. Wu, K. et al. Metamaterial-based real-time communication with high information density by multipath twisting of acoustic wave. *Nat. Commun.* **13**, 5171 (2022).
29. Oh, B., Kim, K., Lee, D. & Rho, J. Engineering metalenses for planar optics and acoustics. *Mater. Today Phys.* **39**, 101273 (2023).
30. Li, Z.-L. et al. Decorated bacteria-cellulose ultrasonic metasurface. *Nat. Commun.* **14**, 5319 (2023).
31. Huang, L. et al. Acoustic resonances in non-Hermitian open systems. *Nat. Rev. Phys.* **6**, 11–27 (2024).
32. Jang, Y., Oh, B., Kim, E. & Rho, J. Bidirectional asymmetric frequency conversion in nonlinear phononic crystals. *Phys. Rev. Lett.* **135**, 036603 (2025).
33. Wang, N. et al. Seven-octave ultrabroadband metamaterial absorbers via quality-factor-weighted mode density modulation. *Natl. Sci. Rev.* **12**, nwaf199 (2025).
34. Sugino, C., Xia, Y., Leadenham, S., Ruzzene, M. & Erturk, A. A general theory for bandgap estimation in locally resonant metastructures. *J. Sound Vibr.* **406**, 104–123 (2017).
35. Zhong, J. et al. Local-nonlinearity-enabled deep subdiffraction control of acoustic waves. *Phys. Rev. Lett.* **131**, 234001 (2023).
36. Dong, E. et al. Soft metalens for broadband ultrasonic focusing through aberration layers. *Nat. Commun.* **16**, 308 (2025).
37. Shen, Y.-X. et al. Ultrasonic super-oscillation wave-packets with an acoustic meta-lens. *Nat. Commun.* **10**, 3411 (2019).
38. Jia, Y. et al. Compact meta-differentiator for achieving isotropically high-contrast ultrasonic imaging. *Nat. Commun.* **15**, 2934 (2024).
39. Nayfeh, A. & Mook, D. *Nonlinear Oscillations* (Wiley, 1995).
40. Yamamoto, T. & Hayashi, S. Combination tones of differential type in nonlinear vibratory systems. *Bull. JSME* **7**, 690–698 (1964).
41. Cheng, Z.-q., Chen, A., Yang, J., Liang, B. & Cheng, J.-c. Broadband achromatic acoustic vortex generator based on integrated-resonant meta-atoms. *Appl. Phys. Lett.* **122**, 183506 (2023).
42. Lee, D. et al. Wide field-of-hearing metalens for aberration-free sound capture. *Nat. Commun.* **15**, 3044 (2024).
43. Weng, J. et al. Meta-neural-network for real-time and passive deep-learning-based object recognition. *Nat. Commun.* **11**, 6309 (2020).
44. Chen, A. et al. Dynamic and high-precision sound manipulation by acoustic metamaterial-empowered phased arrays. *Adv. Funct. Mater.* **35**, 2425833 (2025).
45. Zhang, M. et al. Reconfigurable dynamic acoustic holography with acoustically transparent and programmable metamaterial. *Nat. Commun.* **16**, 9126 (2025).
46. Zeng, L.-S. et al. High-resolution manifold acoustic holography based on high-pixel-array binary metasurfaces. *Adv. Mater.* **37**, 2420229 (2025).
47. Wang, S. et al. A broadband achromatic metalens in the visible. *Nat. Nanotechnol.* **13**, 227–232 (2018).
48. Chen, W. T. et al. A broadband achromatic metalens for focusing and imaging in the visible. *Nat. Nanotechnol.* **13**, 220–226 (2018).
49. Dong, H.-W. et al. Achromatic metasurfaces by dispersion customization for ultra-broadband acoustic beam engineering. *Natl. Sci. Rev.* **9**, nwac030 (2022).

50. Worthington, D. A. et al. Comparing two methods to measure preferred listening levels of personal listening devices. *J. Acoust. Soc. Am.* **125**, 3733–3741 (2009).
51. Fokin, V., Ambati, M., Sun, C. & Zhang, X. Method for retrieving effective properties of locally resonant acoustic metamaterials. *Phys. Rev. B* **76**, 144302 (2007).
52. Fu, Y. et al. Sound vortex diffraction via topological charge in phase gradient metagratings. *Sci. Adv.* **6**, eaba9876 (2020).
53. Červenka, M. & Bednařík, M. Non-paraxial model for a parametric acoustic array. *J. Acoust. Soc. Am.* **134**, 933–938 (2013).
54. Červenka, M. & Bednařík, M. A versatile computational approach for the numerical modelling of parametric acoustic array. *J. Acoust. Soc. Am.* **146**, 2163–2169 (2019).
55. Zhong, J., Kirby, R. & Qiu, X. A spherical expansion for audio sounds generated by a circular parametric array loudspeaker. *J. Acoust. Soc. Am.* **147**, 3502–3510 (2020).
56. *ISO 9613-1:1993 Acoustics – Attenuation of sound during propagation outdoors – Part 1: Calculation of the absorption of sound by the atmosphere* (International Organization for Standardization, 1993).
57. Kim, W., Oh, B., Rho, J. & Moon, W. An accurate measurement of parametric array using a spurious sound filter topologically equivalent to a half-wavelength resonator. *Appl. Acoust.* **240**, 110910 (2025).

Author contributions

W.K., B.O., W.M. and J.R. conceived the idea and initiated the project. W.K. and B.O. performed theoretical analyses. B.O. and W.K. performed numerical simulations. W.K. and B.O. performed the experiments. B.O., W.K. and J.R. mainly wrote the paper. All authors participated in discussions and confirmed the final paper. J.R. and W.M. guided the entire work.

Funding

This work was financially supported by the POSCO-POSTECH-RIST Convergence Research Center program funded by POSCO, and the National Research Foundation (NRF) grant (RS-2024-00356928) funded by the Ministry of Science and ICT (MSIT) of the Korean government. W.K. acknowledges the InnoCORE program (1.260018.01) funded by the MSIT of the Korean government. B.O. acknowledges the NRF Ph.D. fellowship (RS-2024-00409956) funded by the Ministry of Education (MOE) of the Korean government, and the POSTECH Alchemist fellowship.

Competing interests

The authors declare no competing interests.

Additional information

Supplementary information The online version contains supplementary material available at https://doi.org/10.1038/s41467-026-73604-0.

Correspondence and requests for materials should be addressed to Wonkyu Moon or Junsuk Rho.

Peer review information : *Nature Communications* thanks Yuning Guo, Jiaxin Zhong, and the other, anonymous, reviewer for their contribution to the peer review of this work. A peer review file is available.